

A&A 400, 397–413 (2003)
DOI: 10.1051/0004-6361:20021641
© ESO 2003

**Astronomy
&
Astrophysics**

An efficient shock-capturing central-type scheme for multidimensional relativistic flows

II. Magnetohydrodynamics

L. Del Zanna¹, N. Bucciantini¹, and P. Londrillo²

¹ Dipartimento di Astronomia e Scienza dello Spazio, Università degli Studi di Firenze, Largo E. Fermi 2, 50125 Firenze, Italy

² Osservatorio Astronomico di Bologna, Via C. Ranzani 1, 40127 Bologna, Italy

Received 20 September 2002 / Accepted 3 November 2002

Abstract. A third order shock-capturing numerical scheme for three-dimensional special relativistic magnetohydrodynamics (3-D RMHD) is presented and validated against several numerical tests. The simple and efficient *central* scheme described in Paper I (Del Zanna & Bucciantini 2002) for relativistic hydrodynamics is here extended to the magnetic case by following the strategies prescribed for classical MHD by Londrillo & Del Zanna (2000). The scheme completely avoids spectral decomposition into characteristic waves, which is computationally expensive and subject to many degenerate cases in the magnetic case, while it makes use of a two-speed Riemann solver that just requires the knowledge of the two local fast magnetosonic velocities. Moreover, the onset of spurious magnetic monopoles, which is a typical problem for multi-dimensional MHD upwind codes, is prevented by properly taking into account the solenoidal constraint and the specific antisymmetric nature of the induction equation. Finally, the extension to generalized orthogonal curvilinear coordinate systems is included, thus the scheme is ready to incorporate general relativistic (GRMHD) effects.

Key words. magnetohydrodynamics (MHD) – relativity – shock waves – methods: numerical

1. Introduction

Most of the astrophysical sources of high-energy radiation and particles are believed to involve the presence of relativistic motions in *magnetized* plasmas. For example, the radio emission from extra galactic jets (especially from terminal radio lobes) or from plerion-like supernova remnants is due to synchrotron radiation produced by relativistic electrons spiraling around magnetic field lines, thus indicating the presence of significant magnetic fields. Strong magnetic fields are supposed to play an essential role in converting the energy of accreting material around super-massive black holes at the center of Active Galactic Nuclei (AGNs), into powerful relativistic jets escaping along open field lines (Begelman et al. 1984). Similar phenomena may be at work in the galactic compact X-ray sources known as microquasars (Mirabel & Rodriguez 1994). These processes involve the interaction of relativistic gasdynamic flows and shocks with strong magnetic fields, which have now started to be studied via computer simulations (see Meier et al. 2001 for a review). Powerful relativistic blast shocks should also be at the origin of the still mysterious gamma-ray bursts (GRBs; Mészáros & Rees 1992). Moreover, the presence of magnetic fields has been invoked in various astrophysical objects to explain both their morphology and evolution by

applying simplified analytical models to basic plasma physics effects (e.g. the magnetic pinch and kink instabilities may affect the structure of both AGN and microquasar jets, and possibly also the overall shape of pulsar wind nebulae), although a detailed study of the nonlinear and turbulent regimes is still lacking.

Due to the extreme complexity and richness of the possible effects arising in relativistic plasma physics, there is a very strong interest among the astrophysical community in the development of computer codes for both relativistic hydrodynamics (RHD) and magnetohydrodynamics (RMHD), since in most cases only numerical simulations are able to cope with the evolution of such phenomena. After some early attempts based on non-conservative schemes that handled shocks with the aid of large artificial viscosity and resistivity, it is only during the last decade that conservative shock-capturing Godunov-type numerical codes, already successfully applied to gasdynamic problems, have started to be applied to RHD too, achieving both high accuracy in smooth regions of the simulated flow and sharp discontinuous profiles at shocks (e.g. Marquina et al. 1992; Schneider et al. 1993; Balsara 1994; Duncan & Hughes 1994; Eulderink & Mellema 1994; Font et al. 1994; Dolezal & Wong 1995; Falle & Komissarov 1996; Donat et al. 1998; Aloy et al. 1999; Del Zanna & Bucciantini 2002).

Send offprint requests to: L. Del Zanna,
e-mail: ldz@arcetri.astro.it

However, in spite of the success of Godunov-type RHD codes and, at the same time, of the presence of various extensions of gasdynamic schemes to classical MHD (see the recent review by Tóth 2000), to date only a couple of RMHD schemes have been described in the literature. Both codes are second order accurate and are based on linearized Riemann solvers (Roe matrix) in the definition of fluxes at cell interfaces. This process involves the decomposition of primitive variables in a set of *characteristic waves*, each of them propagating a single discontinuity, and a further composition to obtain the numerical upwind fluxes. Moreover, a certain amount of extra artificial viscosity is often needed to stabilize the schemes in particular degenerate cases. The two codes are described in Komissarov (1999a; KO from now on), which is a truly multidimensional scheme, and in Balsara (2001; BA from now on), the latter tested just against one-dimensional (1-D) *shock-tube* problems. There is actually another RMHD code, which has been extensively used in relativistic 2-D and 3-D jet simulations (e.g. Koide et al. 1996; Nishikawa et al. 1998), later extended to general relativistic (GRMHD) effects (with given Schwarzschild or Kerr metrics) and applied to the jet formation mechanism (e.g. Koide et al. 1999, 2000). However, this code cannot be regarded as belonging to the Godunov family, since it is based on a second order Lax-Wendroff scheme, thus with a very high level of implicit numerical viscosity. Moreover, a complete set of the standard numerical tests, needed to check the properties of any shock-capturing scheme, has never been published for such code, so it is difficult to comment on their results and to compare the respective code performances (especially on contact discontinuities, where shock-capturing codes not based on linearized Riemann solvers are usually less accurate).

The reasons behind the difficulty of extending shock-capturing relativistic gasdynamic codes to the magnetic case are essentially the same encountered in building classical MHD schemes, but *amplified*, so to say, by the special relativistic effects. These difficulties may be summarized basically in two classes of problems. The first is concerned with the eigenstructure of the 1-D MHD system, which is much more complex than in the fluid case since now seven characteristic waves are involved and many different degeneracies may occur (depending on the relative orientation of the magnetic and velocity vectors). These problems of *non-strict hyperbolicity* can be cured by accurate re-normalizations of the variables (Brio & Wu 1988; Roe & Balsara 1996), to assure their linear independence, and by introducing additional numerical viscosity in the degenerate cases. The second aspect is more crucial. The multidimensional MHD system, in conservative form, has a specific irreducible structure: the magnetic field (which is a pseudo-vector) is advanced in time by an antisymmetric differential operator, a curl, while all other variables are scalars or vectors advanced in time by a differential operator of divergence form. We notice that this basic duality in the conservation laws of the MHD system is also fully invariant under relativistic coordinate transformations: the covariant evolution equation for \mathbf{B} splits into the classical induction equation and in the non-evolutionary solenoidal $\nabla \cdot \mathbf{B} = 0$ condition.

In numerical schemes where Godunov-type procedures, based on the divergence conservation form and on cell-centered

variables, are also applied to the induction equation, it comes out that magnetic field components develop unphysical discontinuities and numerical monopoles which may grow in time. In RMHD this problem can be relevant: when the magnetic field is very strong, that is when the Alfvén velocity approaches the speed of light, the various eigenvalues collapse one onto the other and it becomes very hard, from a numerical point of view, to distinguish among different physical states: thus, even very small errors in the definition of the magnetic field components, or in the flux derivatives (where the solenoidal condition is implicitly assumed), often lead to unphysical states and to code crashing. Therefore, the proper character of the induction equation and the related preservation of the solenoidal constraint are fundamental issues in numerical RMHD.

To cope with this class of numerical problems, two families of empirical solutions have been proposed: the *cleaning* methods, where the magnetic field components are re-defined at every time step (originally proposed by Brackbill & Barnes 1980, it requires the solution of an additional Poisson equation), and the *eight-wave* method (Powell 1994), which modifies the MHD system by adding a new $\nabla \cdot \mathbf{B}$ variable, to be advected by the flow like the other quantities. These methods may in some cases alleviate (but not solve) the main difficulties. A more consistent way to handle this problem is given by the family of *constrained transport* (CT) methods (first introduced by Evans & Hawley 1988), where the induction equation is correctly discretized to incorporate the solenoidal constraint as a main built-in property. Many schemes (Dai & Woodward 1998; Ryu et al. 1998; Balsara & Spicer 1999b, to cite a few) take advantage of this method, but only in a restricted way, since all basic upwind procedures are still based on the standard (cell-centered) Godunov-type formalism and therefore the production of numerical monopoles is not avoided. A significant further advance has been proposed by KO: after an initial attempt to extend the eight-wave method to RMHD (failed basically because of the above mentioned numerical problems), he finally turns to a CT scheme where the discretized divergence-free magnetic field components are correctly incorporated in the momentum-energy flux functions, although the upwind fluxes for the induction equations are still not properly defined, in our opinion. However, the only astrophysical application of such RMHD code published so far is the propagation of light relativistic jets embedded in a purely toroidal magnetic field (Komissarov 1999b), where the solenoidal condition is actually automatically satisfied for simple geometrical reasons (the field is bound to remain always toroidal), thus this test is not stringent at all for the solenoidal condition preservation problem.

To date, a fully consistent CT-based upwind scheme assuring exact $\nabla \cdot \mathbf{B} = 0$ condition has been proposed by Londrillo & Del Zanna (2000), LD for brevity. In fact, starting from a finite volume formulation of the solenoidal condition and of the induction equation, as in the original CT method, general recipes are given to reconstruct (to any order of accuracy) magnetic field variables at points needed for flux computations and to formulate approximate Riemann solvers also for the induction equations in the CT form. Moreover, as an application, a third order Essentially Non-Oscillatory (ENO) *central*-type scheme was proposed and numerically validated against

various tests. The so-called central schemes do not make use of time-consuming and system-dependent spectral decompositions, and linearized Riemann solvers are replaced by Lax-Friedrichs type averages over the local Riemann fan. In this way, the only characteristic quantities entering the scheme are the local fastest velocities, and also the problems related to the various degeneracies are thus avoided completely. The price to pay is just some additional numerical dissipation at contact and Alfvénic discontinuities, but the high order reconstruction is often able to compensate for these drawbacks.

The central scheme described in LD was applied to the RHD system in Del Zanna & Bucciantini (2002), from now on simply Paper I, where the test simulations presented demonstrated the accuracy and stability of such scheme, even in highly relativistic situations, giving equivalent or better (thanks to its higher order) results than those produced by much more elaborate Godunov-type algorithms. Here the same third order ENO-CT central scheme of LD is extended to the RMHD system, thus this paper may be considered as the generalization of Paper I to the magnetic case. Therefore, both the structure of the paper and the formalism used will be the same as in Paper I, to which the reader will be often referred, especially for some numerical scheme details or for test simulations comparisons. Finally, the CT scheme is extended to generalized orthogonal curvilinear coordinates in the appendix, thus, the inclusion of General Relativity effects with a given metric, i.e. the extension to GRMHD, may be easily achieved (see the appendix of Koide et al. 1999).

2. Ideal RMHD equations

The covariant fluid equations for special relativistic hydrodynamics (RHD) were given in Paper I and here the same notation will be assumed throughout, that is all velocities are normalized against the speed of light ($c = 1$), Greek (Latin) indexes indicate four (three) vectors, $g^{\alpha\beta} = \text{diag}\{-1, 1, 1, 1\}$ is the Minkowski metric tensor (a flat space is assumed here for ease of presentation, for the extension to any set of orthogonal curvilinear coordinates see the appendix), and $x^\alpha = (t, x^j)$ is the four vector of space-time coordinates. The modifications needed to take electromagnetic forces into account are, like in classical MHD, the inclusion of extra terms in the energy-momentum conservation law and a new equation for the magnetic field, to be derived from Maxwell equations. Our derivation follows that of Anile (1989), also described in KO and BA.

Written in terms of the (antisymmetric) electromagnetic tensor $F^{\alpha\beta}$ ($F^{0i} = E_i$, $F^{ij} = B_k$ with $\{i, j, k\} = \{1, 2, 3\}$ and cyclic permutations) and of its dual $F^{*\alpha\beta} = \frac{1}{2}\epsilon^{\alpha\beta\gamma\delta}F_{\gamma\delta}$ ($F^{*0i} = B_i$, $F^{*ij} = -E_k$), where $\epsilon^{\alpha\beta\gamma\delta}$ is the Levi-Civita alternating pseudo-tensor, the covariant Maxwell equations are:

$$\partial_\alpha F^{\alpha\beta} = -J^\beta, \quad \partial_\alpha F^{*\alpha\beta} = 0, \quad (1)$$

where J^α is the four-current containing the source terms, constrained by the condition $\partial_\alpha J^\alpha = 0$, and we have assumed $4\pi \rightarrow 1$. On the other hand, the electromagnetic contribution to the energy-momentum tensor is

$$T_{\text{em}}^{\alpha\beta} = F^\alpha_\gamma F^{\beta\gamma} - \frac{1}{4}g^{\alpha\beta}F_{\gamma\delta}F^{\gamma\delta}, \quad (2)$$

to be added to the fluid part in the conservation law $\partial_\alpha T^{\alpha\beta} = 0$. Finally, we must introduce the covariant relativistic form of Ohm's law in the infinite conductivity approximation, $\mathbf{E} + \mathbf{v} \times \mathbf{B} = 0$, that translates into a condition of vanishing covariant electric field

$$F^{\alpha\beta}u_\beta = 0, \quad (3)$$

where $u^\alpha = (\gamma, \gamma v^j)$ is the four-velocity and $\gamma \equiv u^0 = (1 - v^2)^{-1/2}$ is the Lorentz factor. Note that the other approximation needed to derive the classical MHD equations, namely to neglect the displacement current, is not imposed in RMHD, of course, and the result is that the current, to be derived from the first of Eqs. (1), now depends on the time derivative of the electric field too: $\mathbf{J} = \nabla \times \mathbf{B} - \partial_t \mathbf{E}$.

The equations written so far are not easily compared with their MHD equivalent, due to the presence of the electromagnetic tensor and of its dual, both containing the electric field. However, thanks to Eq. (3), \mathbf{E} may be substituted everywhere by defining a magnetic induction four-vector as $b^\alpha = F^{*\alpha\beta}u_\beta$, that allows to write the electromagnetic tensor in terms of u^α and b^α alone: $F^{\gamma\delta} = \epsilon^{\alpha\beta\gamma\delta}b_\alpha u_\beta$. The components of this new four-vector are

$$b^\alpha = [\gamma(\mathbf{v} \cdot \mathbf{B}), \mathbf{B}/\gamma + \gamma(\mathbf{v} \cdot \mathbf{B})\mathbf{v}], \quad (4)$$

and in the fluid comoving local rest frame we simply have $b^\alpha = (0, \mathbf{B})$. Note the constraints $u_\alpha b^\alpha = 0$ and $|u|^2 \equiv u_\alpha u^\alpha = -1$, so that $|b|^2 \equiv b_\alpha b^\alpha > 0$ and b^α is a space-like vector, with $|b|^2 = B^2/\gamma^2 + (\mathbf{v} \cdot \mathbf{B})^2$.

Thanks to these definitions, the complete set of RMHD equations becomes:

$$\partial_\alpha(\rho u^\alpha) = 0, \quad (5)$$

$$\partial_\alpha[(w + |b|^2)u^\alpha u^\beta - b^\alpha b^\beta + (p + |b|^2/2)g^{\alpha\beta}] = 0, \quad (6)$$

$$\partial_\alpha(u^\alpha b^\beta - u^\beta b^\alpha) = 0, \quad (7)$$

namely the equations of mass conservation, of total energy-momentum conservation, and of magnetic induction. Here $w = e + p$ is the relativistic enthalpy and $e = \rho + p/(\Gamma - 1)$ is the relativistic energy per unit volume for a Γ -law equation of state. Notice the analogy with classical MHD equations, easily obtained by letting $v^2 \ll 1$, while RHD equations are recovered simply by letting $b^\alpha = 0$.

2.1. Evolution equations and the $\nabla \cdot \mathbf{B} = 0$ constraint

Godunov-type shock-capturing numerical methods developed for classical Euler equations apply for any set of hyperbolic conservation laws, and Paper I has shown the application to the RHD case. It is easy to verify that the equations for the fluid variables, Eqs. (5) to (6), retain the usual conservative form:

$$\frac{\partial \mathbf{u}}{\partial t} + \sum_{i=1}^3 \frac{\partial \mathbf{f}^i}{\partial x^i} = 0. \quad (8)$$

Here \mathbf{u} is the vector of conserved variables and \mathbf{f}^i are their corresponding fluxes, along each direction, respectively given by

$$\mathbf{u} = [\rho u^0, w_{\text{tot}} u^0 u^j - b^0 b^j, w_{\text{tot}} u^0 u^0 - b^0 b^0 - p_{\text{tot}}]^T, \quad (9)$$

$$\mathbf{f}^i = [\rho u^i, w_{\text{tot}} u^i u^j - b^i b^j + p_{\text{tot}} \delta^{ij}, w_{\text{tot}} u^0 u^i - b^0 b^i]^T, \quad (10)$$

where we have defined $w_{\text{tot}} = w + |b|^2$ and $p_{\text{tot}} = p + |b|^2/2$.

On the other hand, the equation for b^α , Eq. (7), splits into two parts, which happen to be exactly the same as in classical MHD (this is not surprising since Maxwell equations are Lorentz invariant). The spatial component gives the classical induction equation

$$\frac{\partial \mathbf{B}}{\partial t} + \nabla \times \mathbf{E} = 0; \quad \mathbf{E} = -\mathbf{v} \times \mathbf{B}, \quad (11)$$

which is properly the time evolution equation for \mathbf{B} . Note that the spatial differential operator is in a *curl* form, rather than in a *divergence* form as Eq. (8). This means that the evolution equation of each spatial component of \mathbf{B} has a missing eigen-space, basically due to the antisymmetry of the electromagnetic tensor in Eq. (7), as anticipated in the introduction. Thus, a total of just three independent magnetic fluxes (the electric field vector components, just one in 2-D) are needed for the evolution of \mathbf{B} , while six independent fluxes were required for the momentum evolution. The other consequence of the tensor antisymmetric nature is that the time component of Eq. (7) becomes the usual MHD solenoidal constraint

$$\nabla \cdot \mathbf{B} = 0, \quad (12)$$

which is *not* an evolutionary equation but a differential constraint on the spatial derivatives of \mathbf{B} . This constraint is usually regarded as just an initial condition, since the form of the induction equation assures its preservation in time. Therefore, also numerical schemes must be designed in a way that the specific divergence-free nature of the magnetic field is taken into account as a fundamental constitutive property, otherwise spurious magnetic monopoles will affect the overall solution and often the code stability itself. The CT schemes, and our specific implementation described in Sect. 3, are the class of numerical schemes based on this property.

It is now apparent that Eqs. (11) and (12) are substantially different from the evolutionary conservation laws in Eq. (8). This fundamental constitutional difference, in both the topology of the vector \mathbf{B} field and in its time evolution equation, is better appreciated by introducing the magnetic vector potential \mathbf{A} , defined by $\mathbf{B} = \nabla \times \mathbf{A}$, so that Eq. (12) is automatically satisfied and Eq. (11) takes on the following form (in the Coulomb gauge $\nabla \cdot \mathbf{A} = 0$):

$$\frac{\partial \mathbf{A}}{\partial t} + \mathbf{E} = 0. \quad (13)$$

For a given velocity field (the so-called kinematic approximation), Eq. (13) may be regarded as a set of three-dimensional Hamilton-Jacobi equations, where the \mathbf{E} components are functions of the spatial first derivatives of the \mathbf{A} components. Thus, the overall MHD and RMHD systems are actually combinations of conservative hyperbolic equations and equations of Hamilton-Jacobi kind. It is therefore clear that standard numerical upwind schemes developed for Godunov-type hyperbolic sets of equations *cannot* be applied, and proper upwind expressions for the magnetic flux functions have to be derived.

2.2. Characteristic wave speeds in 1-D RMHD

The one-dimensional case, say $\partial_y = \partial_z = 0$, is, on the other hand, almost perfectly equivalent to the hydrodynamic case and the overall system can be cast in conservative form. In this case Eqs. (11) and (12) yield $B_x = \text{const}$ and Eq. (8) becomes a complete 7×7 system of conservation laws, by just adding the $[B_y, B_z]$ variables to (9) and the fluxes $[-E_z, E_y]$ to (10). However, the 1-D RMHD system, like its MHD counterpart, is not *strictly* hyperbolic, in the sense that two or more eigenvalues may coincide in some degenerate cases, depending on the angle between the direction of propagation and the local magnetic field.

The characteristic structure of this system was first studied by Anile & Pennisi (1987; see also Anile 1989), who derived the eigenvalues and eigenvectors of the associated Jacobian $\partial \mathbf{f} / \partial \mathbf{u}$ by using the covariant notation. All the particular degeneracies were also taken into account.

However, since in our numerical scheme the detailed characteristic eigenstructure is not required, while only the two speeds at the local Riemann fan boundaries need to be computed, here we just report the expressions for the eigenvalues, in the form shown in the appendix of KO. These are one entropy wave

$$\lambda_0 = v_x, \quad (14)$$

two Alfvén waves

$$\lambda_A^\pm = \frac{u^x \pm \tilde{b}^x}{u^0 \pm \tilde{b}^0}, \quad (15)$$

and four magneto-sonic waves (two fast and two slow waves), that unfortunately do not have a simple analytical expression and must be derived from the nonlinear quartic equation

$$(1 - \varepsilon^2)(u^0 \lambda - u^x)^4 + (1 - \lambda^2) \left[c_s^2 (\tilde{b}^0 \lambda - \tilde{b}^x)^2 - \varepsilon^2 (u^0 \lambda - u^x)^2 \right] = 0, \quad (16)$$

where $c_s^2 = \Gamma p/w$ is the sound speed squared, $\tilde{b}^\alpha = b^\alpha / \sqrt{w_{\text{tot}}}$ ($|\tilde{b}|^2 = \tilde{b}_\alpha \tilde{b}^\alpha = |b|^2/w_{\text{tot}}$), and $\varepsilon^2 = c_s^2 + |\tilde{b}|^2 - c_s^2 |\tilde{b}|^2$. Note that the ordering of MHD characteristic speeds and the various degeneracies are preserved in the relativistic case (Anile 1989), although the symmetry between each λ^\pm couple of waves is lost, due to relativistic aberration effects.

Several numerical algorithms may be employed to solve Eq. (16): Newton's root finding technique, applied in the proper interval for each characteristic speed, Laguerre's method for polynomials, involving complex arithmetics, or eigenvalues finding routines, based on the associated *upper Hessenberg* matrix. We have tested all these numerical methods by using the *Numerical Recipes* (Press et al. 1986) appropriate routines, which are *rtsafe*, *zroots*, and *hqr*, respectively, under a wide range of conditions, including various degenerate cases and ultra-relativistic speeds, temperatures or magnetic fields. However, in the code we have decided to adopt the analytical approach, described for example in Abramowitz & Stegun (1965), which requires in turn the analytical solution of a cubic and of two quadratic algebraic equations. We have found that this algorithm gives results comparable to Laguerre's or

the matrix methods, the most robust and precise ones, and it is much less computationally expensive. On the other hand, Newton's iterative method, which is the fastest in normal conditions, was found to fail in some nearly degenerate cases.

2.3. Primitive variables

In order to compute fluxes, the vector of primitive fluid variables $\mathbf{v} = [\rho, v^j, p]^T$ have to be recovered from the conservative ones $\mathbf{u} = [D, Q^j, E]^T$, defined in Eq. (9), at the beginning of every numerical time step (please notice that in the present sub-section E will indicate the total energy, which has nothing to share with the electric field \mathbf{E}). Like for RHD codes, this procedure must be carried out by some iterative root-finding routine. In the magnetic case this process is even more difficult, in spite of the fact that \mathbf{B} can be considered as given (its components are both primitive and conserved variables). In BA the full 5×5 system is solved by inverting the $\mathbf{u}(\mathbf{v}) = 0$ set of nonlinear equations as they stand, providing also all the partial derivatives needed. However, we have verified that this process is neither efficient nor stable when relativistic effects are strong. In Koide et al. (1996) and KO the system to solve was reduced down to a couple nonlinear equations, while here we manage to derive just *one* nonlinear equation to be solved iteratively, with obvious improvements both in terms of speed and precision.

The first step is to use the definitions of u^α and b^α to write the known conservative variables $\mathbf{u} = [D, Q^j, E]^T$ in terms of the primitive variables. The vector \mathbf{Q} becomes

$$\mathbf{Q} = (W + B^2)\mathbf{v} - (\mathbf{v} \cdot \mathbf{B})\mathbf{B}, \quad (17)$$

and by taking the projection along \mathbf{B} we find the important relation $S \equiv (\mathbf{Q} \cdot \mathbf{B}) = W(\mathbf{v} \cdot \mathbf{B})$, where like in Paper I we have used $W = w\gamma^2$, $w = \rho + \Gamma_1 p$, and $\Gamma_1 = \Gamma/(\Gamma - 1)$.

A 2×2 system of nonlinear equations is then derived by taking the square of Eq. (17) and by using the equation for the total energy E :

$$W^2 v^2 + (2W + B^2)B^2 v_\perp^2 - Q^2 = 0, \quad (18)$$

$$W - p + \frac{1}{2}B^2 + \frac{1}{2}B^2 v_\perp^2 - E = 0, \quad (19)$$

where $B^2 v_\perp^2 \equiv B^2 v^2 - (\mathbf{v} \cdot \mathbf{B})^2 = B^2 v^2 - S^2/W^2$. If we then use the relations

$$\rho = D\sqrt{1 - v^2}, \quad p = [(1 - v^2)W - \rho]/\Gamma_1, \quad (20)$$

it comes out that all quantities appearing in the system are written in terms of the two unknowns v^2 (or equivalently γ) and W . Once these variables are found numerically, primitive quantities will be easily derived through Eqs. (20) and by inverting Eq. (17), that is

$$\mathbf{v} = \frac{1}{W + B^2} \left(\mathbf{Q} + \frac{S}{W} \mathbf{B} \right). \quad (21)$$

In order to bring the system down to just a single nonlinear equation (to be solved numerically, for example by Newton's iterative method), we found it useful to define $B^2 v_\perp^2 = T^2/(W + B^2)^2$ in Eqs. (18) and (19), where $T^2 \equiv B^2 Q^2 - S^2$ is a new, but given, parameter. Then we write Eq. (19) as a third order

algebraic equation for W with coefficients that depend on v^2 alone

$$\left[\left(1 - \frac{1 - v^2}{\Gamma_1} \right) W - E + \frac{\rho}{\Gamma_1} + \frac{B^2}{2} \right] (W + B^2)^2 + \frac{T^2}{2} = 0, \quad (22)$$

which can be solved analytically (again, see Abramowitz & Stegun 1965). Note that the cubic polynomial on the left hand side has a positive local maximum in $W = -B^2$. Thus, since we know that at least one root must be positive, all the three roots of Eq. (22) are actually bound to be real, and we have verified that the largest one always yields the correct result.

The function $W(\xi)$, with $\xi = v^2$, is thus available together with its derivative $W'(\xi)$, so the final step is to apply Newton's method to find the root of $\mathcal{F}(\xi) = 0$, where

$$\mathcal{F}(\xi) = W^2 \xi + (2W + B^2) \frac{T^2}{(W + B^2)^2} - Q^2, \quad (23)$$

and

$$\mathcal{F}'(\xi) = W^2 + 2WW' \left[\xi - \frac{T^2}{(W + B^2)^3} \right]. \quad (24)$$

The numerical routine actually employed in the code is *rtsafe* (Press et al. 1986), which applied with an accuracy of 10^{-6} in the range $\xi_{\min} = 0$ and $\xi_{\max} = 1 - 10^{-6}$ ($\gamma_{\max} = 1000$), typically converges in 5–10 iterations for any set of conservative variables and magnetic field components that actually admits a solution.

The technique described above appears to be extremely efficient and, above all, robust; we therefore recommend its use in all RMHD shock-capturing codes, whatever the numerical scheme actually employed.

3. The finite-difference ENO-CT central scheme

In the present section the third order ENO-CT scheme described in LD will be adapted and applied to the RMHD equations derived above. The ENO-CT scheme employs a finite-difference discretization framework, and uses *Convex* ENO (CENO) reconstruction procedures to get high order non-oscillatory point values of primitive variables needed to compute numerical flux derivatives. The upwind procedures in numerical fluxes are based on approximate Riemann solvers of the Lax-Friedrichs type, as in other central schemes. In particular, here we adopt a flux formula based on *two* local characteristic speeds, rather than just one as in the code discussed in LD. The scheme will be here presented in the semi-discrete formalism, that is time dependency is implicitly assumed for all spatially discretized quantities. The evolution equations are then integrated in time by applying a third order TVD Runge-Kutta algorithm (Shu & Osher 1988), with a time-step inversely proportional to the largest (in absolute value) of the characteristic speeds (the magneto-sonic velocities defined in Sect. 2.2) present in the domain and subject to the CFL condition. The reader is referred to both LD and Paper I for further numerical references and comments. In any case, see Shu (1997) for a general overview of ENO schemes, Liu & Osher (1998) for the original formulation of the CENO central scheme, and

Kurganov et al. (2001) for the introduction of two-speed averaged Riemann solvers in high order central schemes for both hyperbolic and Hamilton-Jacobi equations.

3.1. Discretization of fluid and magnetic variables

Given a Cartesian uniform 3-D mesh of $N_x \times N_y \times N_z$ cells (volumes), with sizes Δx , Δy , and Δz , let us indicate with $P_{i,j,k} \equiv (x_i, y_j, z_k)$ the cell centers and with $P_{i+1/2,j,k}$ the points centered on intercell surfaces (along x in this case). Classical Godunov-type schemes are usually formulated in a finite-volume (FV) framework, where state variables are advanced in time as cell averaged values. By applying Gauss' theorem to Eq. (8), the time evolution equation for the vector of *fluid* variables becomes

$$\frac{d}{dt} \bar{u} = - \sum_{i=1}^3 \frac{\Delta_i \bar{f}^i}{\Delta x^i}, \text{ at } P_{i,j,k}, \quad (25)$$

where, for each scalar variable, $\bar{u} \equiv \bar{u}_{i,j,k}$ is the FV cell averaged discretization of $u(\mathbf{x})$ at $P_{i,j,k}$. Flux derivatives are given in conservative form as simple two-point differences of the numerical fluxes \bar{f}^i . These fluxes are defined as intercell surface averages and are stored on surface centers, each in the direction corresponding to the i component, with $i = 1, 2, 3$. For example, $\bar{f} = \bar{f}^x$ is located on $P_{i+1/2,j,k}$ points, and the Δ_x operator, centered in $P_{i,j,k}$, is defined as

$$[\Delta_x \bar{f}]_{i,j,k} = \bar{f}_{i+1/2,j,k} - \bar{f}_{i-1/2,j,k}. \quad (26)$$

Similar expressions hold in the other directions.

A different strategy is needed to reconstruct the magnetic field variables. The induction Eq. (11) is in curl form, thus the correct procedure for discretization in the FV framework is the application of Stokes' theorem. The x component gives

$$\frac{d}{dt} \bar{B}_x = - \frac{\Delta_y \bar{E}_z}{\Delta y} + \frac{\Delta_z \bar{E}_y}{\Delta z}, \text{ at } P_{i+1/2,j,k}, \quad (27)$$

where \bar{B}_x is discretized as *surface* average and located at $P_{i+1/2,j,k}$ intercell points, while for example \bar{E}_z is a *line* average and is located at $P_{i+1/2,j+1/2,k}$ volume *edge* points (cell corners in 2-D). Similar expressions are defined for the y and z components. Thanks to the above discretization, it is straightforward to prove that the numerical solenoidal condition will be algebraically satisfied at all times (if satisfied at $t = 0$):

$$\frac{d}{dt} \left(\frac{\Delta_x \bar{B}_x}{\Delta x} + \frac{\Delta_y \bar{B}_y}{\Delta y} + \frac{\Delta_z \bar{B}_z}{\Delta z} \right) \equiv 0, \text{ at } P_{i,j,k}. \quad (28)$$

This is the fundamental property of the CT method and relies on the definition of the staggered field components

$$[\bar{B}_x]_{i+1/2,j,k}, [\bar{B}_y]_{i,j+1/2,k}, [\bar{B}_z]_{i,j,k+1/2} \quad (29)$$

as primary data. It is important to notice that these data contain essential informations not only for the discretization of the corresponding variables at cell centers, but also for the definition of longitudinal derivatives at the same points, since two values per cell are available for each component.

A first consequence is that a *continuous* numerical vector potential \bar{A} can be derived in a unique way by inverting the discretized form of the $\nabla \times \mathbf{A} = \mathbf{B}$ relation. By applying Stokes' theorem once more it is easy to verify that these data must be defined as line averages along the longitudinal direction and stored at the same locations as the corresponding electric field \bar{E} components. On the other hand, if the \bar{A} components are used as primary data, then the time evolution discretized equations in Eq. (27) must be replaced by

$$\frac{d}{dt} \bar{A}_x = -\bar{E}_x \text{ at } P_{i,j+1/2,k+1/2}, \quad (30)$$

and similarly for the other components. The field components in Eq. (29) are then derived as

$$\bar{B}_x = \frac{\Delta_y \bar{A}_z}{\Delta y} - \frac{\Delta_z \bar{A}_y}{\Delta z} \text{ at } P_{i+1/2,j,k}, \quad (31)$$

and similarly for the y and z components. In the CT framework, the two choices are perfectly equivalent, and the solenoidal constraint Eq. (28) is still clearly satisfied exactly.

A second main property is given by the continuity condition of the face averaged components (i.e. the numerical magnetic fluxes) in Eq. (29). For example, the numerical function

$$\bar{B}_x(x) = \frac{1}{S} \int_S B_x(x) dS, \quad (32)$$

is a continuous function of x , where S is a cell section normal to the x direction. A simple proof is given by integrating $\nabla \cdot \mathbf{B} = 0$ on a volume including S and tending to it by letting $\Delta x \rightarrow 0$ (see LD). Therefore, at points of discontinuity (intercell surfaces) staggered data are well defined as point values in the corresponding longitudinal direction, having a single-state numerical representation there (this fundamental property will be fully appreciated later on for upwind calculations) and showing at most discontinuous first derivatives along the corresponding coordinate.

In our ENO-CT scheme, the FV discretization is replaced by a *finite-difference* (FD) discretization based on point values, which is more efficient in the multi-dimensional case and allows to use just 1-D interpolation routines. The primary data actually employed in our scheme are thus the point-valued \mathbf{u} fluid variables, defined at cell centers $P_{i,j,k}$, and the point-valued potential vector \mathbf{A} components, located at cell edges exactly as in the FV approach. The time evolution equations are thus, in the FD CT scheme

$$\frac{d}{dt} \mathbf{u} = - \sum_{i=1}^3 \frac{\Delta_i \hat{f}^i}{\Delta x^i}, \text{ at } P_{i,j,k}, \quad (33)$$

and

$$\begin{aligned} (d/dt)A_x &= -E_x, \text{ at } P_{i,j+1/2,k+1/2}, \\ (d/dt)A_y &= -E_y, \text{ at } P_{i+1/2,j,k+1/2}, \\ (d/dt)A_z &= -E_z, \text{ at } P_{i+1/2,j+1/2,k}, \end{aligned} \quad (34)$$

where now the numerical fluid flux functions \hat{f}^i are such that their volume average approximate the FV fluxes \bar{f}^i to the given order of accuracy, while electric fields in the FD formalism are

simply point-valued numerical functions. Eqs. (33) and (34) are thus the time evolution equations that are integrated by the Runge-Kutta time-stepping algorithm. The reconstruction procedures and the upwind formulae to define numerical fluxes \hat{f}^i and \mathbf{E} , in the respective locations, are given in the following sub-sections.

3.2. Reconstruction procedures

At this preliminary level of analysis, everything is exact. Approximations come into play only in the reconstruction procedures, when point values needed for flux computations are recovered from primary numerical data to some accuracy level. At a second order approximation, the procedures are straightforward, since the two discretization approaches, FV and FD, coincide. At higher order of accuracy, on the other hand, specific procedures must be defined.

The first step is to derive magnetic field components from vector potential data. This is done in our scheme at the beginning of each time-stepping sub-cycle. To third order accuracy, we first define

$$\begin{aligned}\hat{A}_x &= [1 - \gamma_1 \mathcal{D}_y^{(2)} - \gamma_1 \mathcal{D}_z^{(2)}]A_x, \text{ at } P_{i,j+1/2,k+1/2}, \\ \hat{A}_y &= [1 - \gamma_1 \mathcal{D}_z^{(2)} - \gamma_1 \mathcal{D}_x^{(2)}]A_y, \text{ at } P_{i+1/2,j,k+1/2}, \\ \hat{A}_z &= [1 - \gamma_1 \mathcal{D}_x^{(2)} - \gamma_1 \mathcal{D}_y^{(2)}]A_z, \text{ at } P_{i+1/2,j+1/2,k},\end{aligned}\quad (35)$$

where $\gamma_1 = 1/24$ and $\mathcal{D}^{(2)}$ is the non-oscillatory numerical second derivative defined in Paper I. Then the divergence-free magnetic field components are derived directly from the high order approximation of $\mathbf{B} = \nabla \times \mathbf{A}$, which gives

$$\begin{aligned}\hat{B}_x &= (\Delta_y \hat{A}_z) / \Delta y - (\Delta_z \hat{A}_y) / \Delta z, \text{ at } P_{i+1/2,j,k}, \\ \hat{B}_y &= (\Delta_z \hat{A}_x) / \Delta z - (\Delta_x \hat{A}_z) / \Delta x, \text{ at } P_{i,j+1/2,k}, \\ \hat{B}_z &= (\Delta_x \hat{A}_y) / \Delta x - (\Delta_y \hat{A}_x) / \Delta y, \text{ at } P_{i,j,k+1/2}.\end{aligned}\quad (36)$$

These new staggered field components clearly satisfy, at all times t :

$$\frac{\Delta_x \hat{B}_x}{\Delta x} + \frac{\Delta_y \hat{B}_y}{\Delta y} + \frac{\Delta_z \hat{B}_z}{\Delta z} \equiv 0, \text{ at } P_{i,j,k},\quad (37)$$

which is the point-value equivalent expression of Eq. (28). Thus, in the FD version of the CT scheme, the fundamental divergence-free magnetic components are those defined in Eq. (36), whose divided differences directly give high order approximations of the longitudinal derivative.

Having assured approximated first derivatives satisfying exact divergence-free relations, it is now possible to reconstruct the corresponding point values in the longitudinal coordinate, which will be needed for the definition of numerical fluxes, in a way to maintain the value of the first derivative. Since only one-dimensional operators, in turn, are now required, we denote by B the unknown point-value numerical data and by \hat{B} the data derived just above, where both sets are located at the same intercell points. By definition, to third order approximation we have

$$[1 - \gamma_1 \mathcal{D}^{(2)}]B = \hat{B}.\quad (38)$$

For a given set of values \hat{B} , one has then to invert the $\mathcal{D}^{(2)}$ operator, which is not based on a fixed stencil of data and the resulting matrix appears then to be highly non-linear. However, the operator on the left hand side can be inverted in an explicit way by using the Taylor expansion $[1 - \gamma_1 \mathcal{D}^{(2)}]^{-1} \simeq 1 + [\gamma_1 \mathcal{D}^{(2)}] + [\gamma_1 \mathcal{D}^{(2)}]^2 + \dots$, so that the component B may be approximated by a finite order iteration as

$$B^{(n)} = \hat{B} + [\gamma_1 \mathcal{D}^{(2)}]B^{(n-1)}; \quad B^{(0)} = \hat{B}.\quad (39)$$

It is essential to notice that the approximation order of the B point values does not increase with the iteration number n , being always of the third order of the base scheme. What changes is the residual error in the related solenoidal condition: usually $n = 5$ iterations are enough to assure the preservation of the longitudinal derivative value, so that Eq. (37) remains exact within machine accuracy in the computation of flux derivatives too, thus avoiding spurious monopoles terms in the dynamical equations.

A final interpolation step is needed to define point-value magnetic field \mathbf{B} components at cell centers $P_{i,j,k}$, where fluid conservative variables \mathbf{u} are stored. Thus, at the beginning of each time sub-cycle, point-value primitive variables $\mathbf{v} = [\rho, v^j, p]^T$ can be recovered as described in Sect. 2.3.

In order to use these variables in the definition of numerical fluxes, a reconstruction step is required along each direction, to provide point-value data at intercell points. For multi-dimensional calculations and for higher than second order schemes, like in our case, the reconstruction routines are one-dimensional only in the FD framework, which is then to be preferred. Moreover, the reason for reconstructing the primitive variables is also apparent: if reconstruction were applied to conservative variables, then the time-consuming (in RMHD) algorithm of Sect. 2.3 would be needed at intercell points for each direction. The reconstruction routines employed in our code are the Convex ENO procedures described in Paper I, with a choice of two slope limiters (MinMod and Monotonized Centered) to prevent unwanted oscillations and to preserve monotonicity.

Reconstruction procedures at intercell locations give two-state, left (L) and right (R), reconstructed variables, depending on the stencil used in the definition of the (quadratic) interpolation polynomial. However, not all the eight variables retain such two-state representation, since we know from Eq. (32) that the longitudinal field component along the direction of flux differentiation must be continuous at corresponding intercell locations, and this property is preserved also for point-value staggered \mathbf{B} components defined through Eq. (39). Therefore, the longitudinal field is not reconstructed as the other seven Godunov variables, and the single-state value provided by Eq. (39) is assumed in flux calculations. Notice that this is the crucial point discussed in the introduction: the use of the divergence-free field components in numerical fluxes permits to avoid the onset of spurious monopoles in the computation of the right-hand side of Eq. (33).

Finally, point-value numerical fluxes f defined at intercell locations (the proper upwind procedures to define them will be discussed in the following sub-section) have to be further transformed in the corresponding \hat{f} fluxes defined in Eq. (33).

This step is required to approximate flux derivatives to higher than second order. To third order accuracy we have, as usual

$$\hat{f} = [1 - \gamma_1 \mathcal{D}^{(2)}]f, \quad (40)$$

whereas this final step is not needed for electric fields, which are defined in Eqs. (34) as point-value data.

3.3. Central-upwind numerical fluxes

In Lax-Friedrichs central-type schemes, two couples of characteristic velocities λ_{\pm}^L and λ_{\pm}^R are first defined at intercell locations. These velocities, which are the fast magneto-sonic speeds in RMHD, are those at the boundaries of the two local Riemann fans (one fan for each L or R state), and are derived by using the procedure described in Sect. 2.2. Then a local averaged Riemann problem is solved by using either the two-speed HLL (from Harten, Lax, and van Leer) or the single-speed LLF (local Lax-Friedrichs) flux formulae:

$$f^{\text{HLL}} = \frac{\alpha^+ f^L + \alpha^- f^R - \alpha^+ \alpha^- (\mathbf{u}^R - \mathbf{u}^L)}{\alpha^+ + \alpha^-}, \quad (41)$$

$$f^{\text{LLF}} = \frac{1}{2} [f^L + f^R - \alpha (\mathbf{u}^R - \mathbf{u}^L)], \quad (42)$$

where

$$\alpha^{\pm} = \max\{0, \pm \lambda_{\pm}^L, \pm \lambda_{\pm}^R\}; \quad \alpha = \max\{\alpha^+, \alpha^-\}, \quad (43)$$

where basically all the other intermediate states are averaged out. Notice that when the local Riemann fan is symmetric, then $\alpha^+ = \alpha^- = \alpha$ and the two fluxes coincide, whereas, when both fast magneto-sonic speeds have the same sign one of the α^{\pm} is zero and the HLL flux becomes a pure upwind flux, either f^L or f^R . This is why the HLL scheme described above was defined in Kurganov et al. (2001) as *central-upwind*.

The upwind states for the numerical \mathbf{E} flux functions of the induction equation are defined by the same averaged Riemann solver, now to be applied to flux functions having a base four-state structure. This different structure arises because at cell edges, where the electric fields must be defined, *two* surfaces of discontinuity intersect, and modes of Riemann fans coming from different directions overlap there. A proper expression that extends Eqs. (41) and (42) to the induction equation fluxes is derived by taking advantage of the analytical and numerical experience developed for the Hamilton-Jacobi equations. For ease of presentation, only the z component of the electric field, $E_z = -(v_x B_y - v_y B_x)$ (that usually needed in 2-D simulations), will be treated here, while the x and y components are easily obtained by cyclic permutations of the indexes.

Let us indicate with double upper indexes these four states, where the first refers to upwinding along x and the second along y , obtained by reconstructing the required primitive variables at the edge point $P_{i+1/2, j+1/2, k}$ by applying a sequence of two independent one-dimensional reconstruction routines. For each component of the magnetic field just one reconstruction in the transverse direction is actually required, of course.

The proposed HLL and LLF upwind formulae for the E_z flux function are given respectively by

$$E_z^{\text{HLL}} = \frac{\alpha_x^+ \alpha_y^+ E_z^{\text{LL}} + \alpha_x^+ \alpha_y^- E_z^{\text{LR}} + \alpha_x^- \alpha_y^+ E_z^{\text{RL}} + \alpha_x^- \alpha_y^- E_z^{\text{RR}}}{(\alpha_x^+ + \alpha_x^-)(\alpha_y^+ + \alpha_y^-)} + \frac{\alpha_x^+ \alpha_x^-}{\alpha_x^+ + \alpha_x^-} (B_y^{\text{R}} - B_y^{\text{L}}) - \frac{\alpha_y^+ \alpha_y^-}{\alpha_y^+ + \alpha_y^-} (B_x^{\text{R}} - B_x^{\text{L}}), \quad (44)$$

$$E_z^{\text{LLF}} = \frac{1}{4} (E_z^{\text{LL}} + E_z^{\text{LR}} + E_z^{\text{RL}} + E_z^{\text{RR}}) + \frac{1}{2} \alpha_x (B_y^{\text{R}} - B_y^{\text{L}}) - \frac{1}{2} \alpha_y (B_x^{\text{R}} - B_x^{\text{L}}). \quad (45)$$

The α_x^{\pm} and α_y^{\pm} at $P_{i+1/2, j+1/2, k}$ required above should be calculated by taking the maximum characteristic speed (in absolute value) among the four reconstructed states, whereas for sake of efficiency we actually consider the maximum over the two neighboring inter-cell points, where these speeds had been already calculated for fluid fluxes. As usual, the LLF numerical flux is obtained from the HLL one by letting $\alpha_x^+ = \alpha_x^- = \alpha_x$ and $\alpha_y^+ = \alpha_y^- = \alpha_y$.

Note that for a pure 2-D case $\partial_x A_z = -B_y$ and $\partial_y A_z = +B_x$, thus for a given velocity field the induction equation simply becomes the Hamilton-Jacobi equation $(d/dt)A_z = -E_z(\partial_x A_z, \partial_y A_z)$ and our upwind formulae correctly match in this case with those given in Kurganov et al. (2001), where the HLL central-upwind scheme was applied to this kind of equations. Moreover, notice that for discontinuity surfaces coincident with one of the inter-cell boundaries, that is for 1-D situations, Eqs. (44) and (45) reduce respectively to Eqs. (41) and (42), as it should be. Thus, for 2-D or 1-D calculations, our 3-D ENO-CT scheme automatically treats the magnetic field components which does not require a Hamilton-Jacobi formulation in the usual Godunov-type approach.

The fact that the magnetic numerical fluxes for the induction equation must use upwind formulae based on four-state quantities seems to have been overlooked by the other authors, who generally just *interpolate* the x and y 1-D single-state upwind fluxes already calculated at intercell points to the cell corner where E_z must be defined (we specialize here to a 2-D situation). However, this procedure is clearly incorrect, because at cell corners only B_x and B_y have a two-state representation, whereas v_x and v_y retain the complete four-state representation.

4. Numerical results

The numerical verification of the code is reported here in three separate sub-sections: 1-D shock tubes are presented in the first, some 2-D test simulations of astrophysical interest are shown in the second, while the third subsection is devoted to more quantitative tests concerning code convergence on smooth fields in both 1-D and 2-D.

Since in 1-D RMHD the solenoidal constraint is automatically satisfied and transverse magnetic field components behave essentially like the other conservative variables, the shock tube tests shown here just illustrate the ability of the code to handle degenerate cases (where the system is no longer strictly hyperbolic due to the coincidence of two or more eigenvalues)

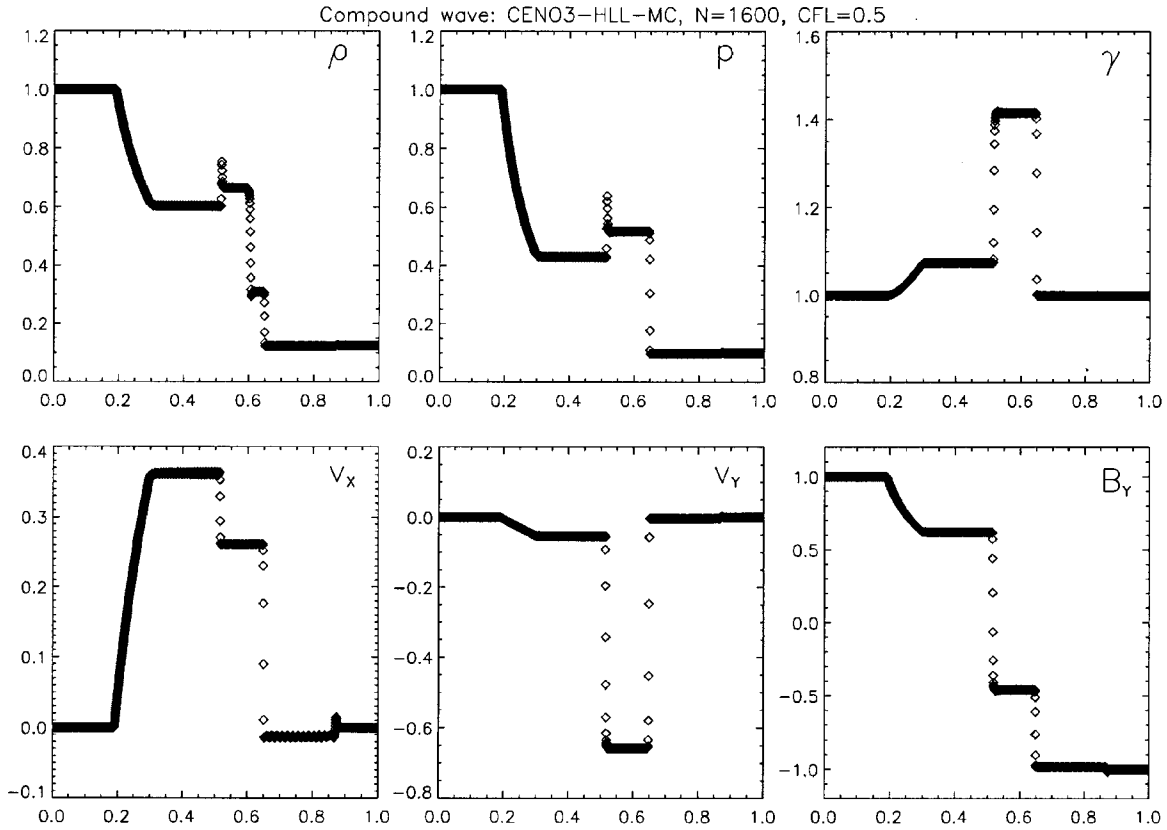


Fig. 1. The relativistic analog of Brio & Wu (1988) MHD test problem involving a compound wave. If compared to BA, our left moving compound shock and right moving slow shock are better resolved. Here the base scheme CENO3-HLL-MC is used, with $N = 1600$ grid points to compare with BA and Courant number $CFL = 0.5$.

and to separate the various Riemann discontinuities or rarefaction waves, which are more numerous in the magnetized case (up to seven) rather than in the fluid case (just three). On the other hand, multidimensional tests truly prove the robustness of the code and its accuracy in preserving $\nabla \cdot \mathbf{B} = 0$ in time, thus avoiding the onset of spurious forces due to the presence of numerical magnetic monopoles. The solenoidal constraint is preserved within machine accuracy, like for all CT schemes, and therefore the spatial distribution of $\nabla \cdot \mathbf{B}$ and its evolution in time will not be shown (however, see LD for proofs in classical MHD tests).

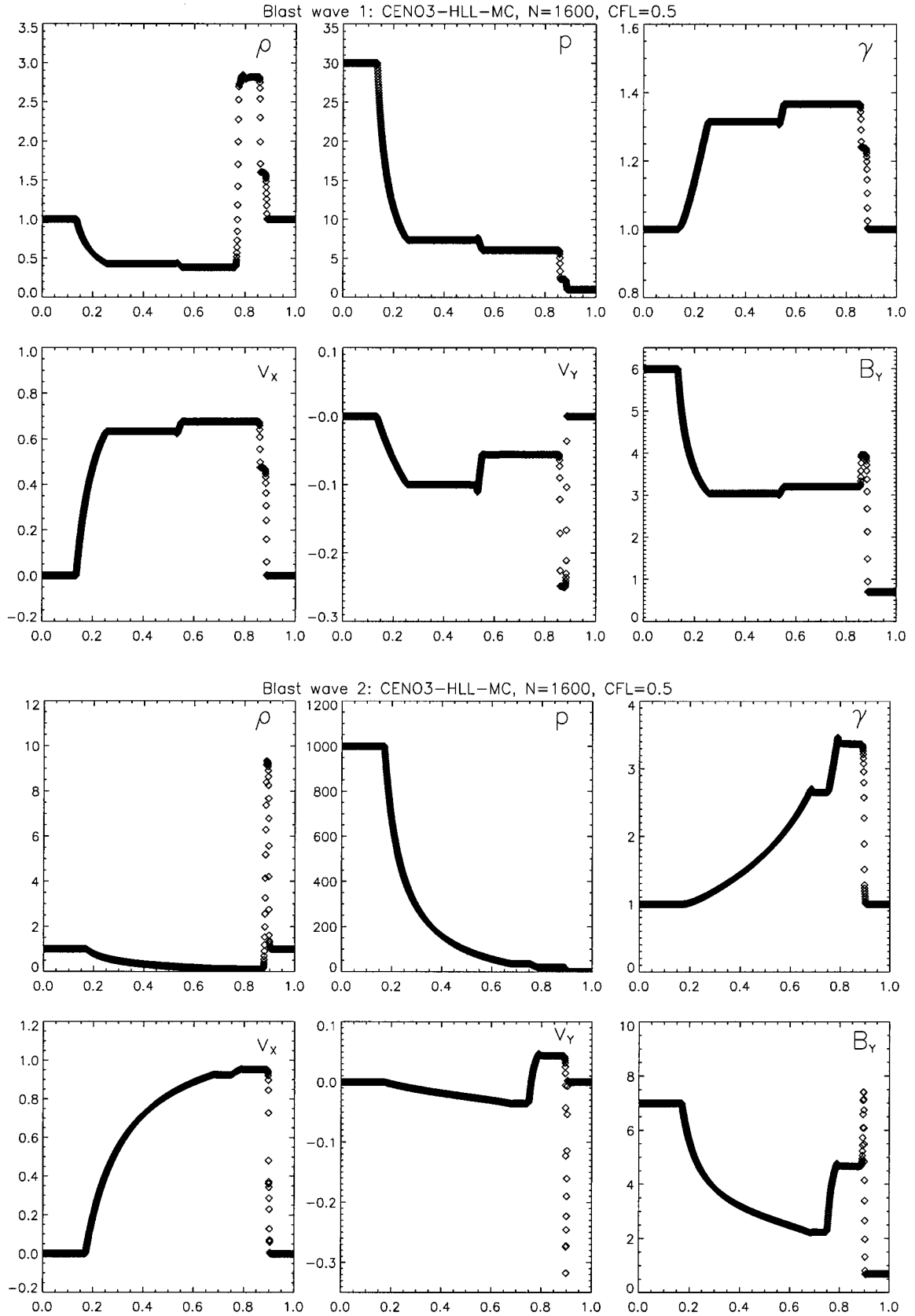
For all the simulations that we will show, the scheme described above is applied without any additional numerical viscosity term, which are instead introduced by both KO and BA in order to stabilize their Roe-type codes. The numerical parameters that may be changed in our simulations are just the CFL number (here always $c = 0.5$), the reconstruction slope limiter (the Monotonized Centered, MC, or the most smearing MinMod, MM, for the multidimensional highly relativistic tests shown below; see Paper I for the precise definition of these limiters), the order of the reconstruction (third, with CENO routines, whenever possible), and the central-type averaged Riemann solver (we always use the HLL solver). Concerning this last point, we have verified that HLL and LLF actually give almost identical results in all simulations. This is easily explained: in RMHD either the sound speed or the Alfvén speed

are often high, especially at shocks where upwinding becomes important, so that $\alpha^+ \sim \alpha^- \sim \alpha \sim 1$ and the two fluxes tend to coincide.

4.1. One-dimensional tests

Shock-tube Riemann problems are not really suited for high order shock capturing codes, because oscillations may easily appear near discontinuities. This is especially true when the reconstruction is not applied to characteristic waves, because the various contributions cannot be singled out and, for example, it is impossible to steepen numerically contact or Alfvénic discontinuities. However, we will see here that the base third order CENO3-HLL-MC scheme is able to treat this kind of problems reasonably well, usually achieving similar or even better accuracy than characteristics-based second order schemes. In Table 1 the parameters for the initial left (L) and right (R) states of the proposed Riemann problems are reported (in all cases $v_y = v_z = 0$, $\Gamma = 5/3$ and $t = 0.4$). These are the same tests as in BA, except the first where $\Gamma = 2$ was used. Moreover, for ease of comparison, the same resolution used in BA, $N = 1600$ grid points, is employed.

The results relative to the first test are shown in Fig. 1. This is the relativistic extension of the classic Brio & Wu (1988) test, where a *compound*, or intermediate, shock wave is formed. There is still a debate going on about the reality of



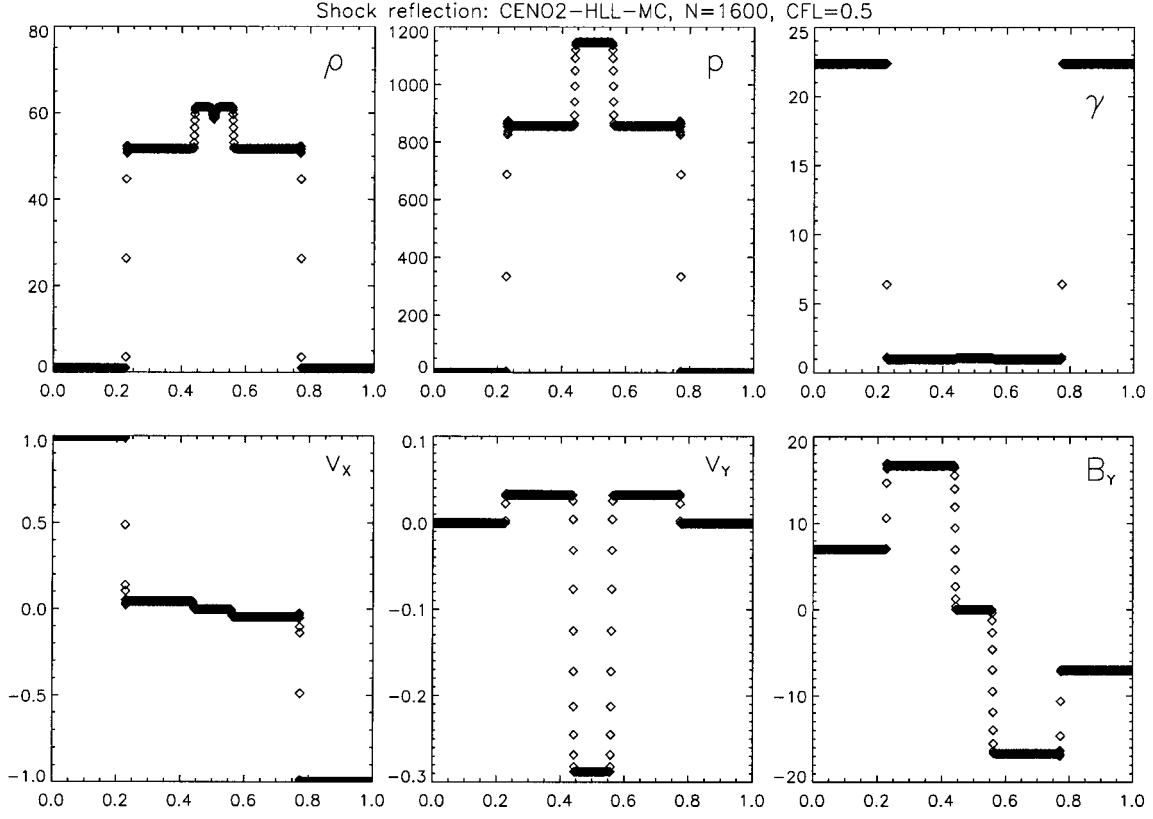


Fig. 3. The relativistic MHD shock reflection problem, with $\gamma \approx 22.4$ flows colliding at $x = 0.5$. This test is crucial for two reasons: the post-shock oscillations, here damped by reconstructing at second order, and the *wall heating* problem, that appears to be quite reduced by the use of HLL.

Table 1. Constant left (L) and right (R) states for the Riemann problems.

| Test | ρ | v_x | p | B_x | B_y | B_z |
|------|--------|--------|--------|-------|-------|-------|
| 1 L | 1.0 | 0.0 | 1.0 | 0.5 | 1.0 | 0.0 |
| 1 R | 0.125 | 0.0 | 0.1 | 0.5 | -1.0 | 0.0 |
| 2 L | 1.0 | 0.0 | 30.0 | 5.0 | 6.0 | 6.0 |
| 2 R | 1.0 | 0.0 | 1.0 | 5.0 | 0.7 | 0.7 |
| 3 L | 1.0 | 0.0 | 1000.0 | 10.0 | 7.0 | 7.0 |
| 3 R | 1.0 | 0.0 | 0.1 | 10.0 | 0.7 | 0.7 |
| 4 L | 1.0 | 0.999 | 0.1 | 10.0 | 7.0 | 7.0 |
| 4 R | 1.0 | -0.999 | 0.1 | 10.0 | -7.0 | -7.0 |

such structures, invariably found by any shock-capturing code but not predicted by analytic calculations (e.g. Barmin et al. 1996; Myong & Roe 1998). However, it is not our intention to contribute to that debate, here we just want to show that our third order reconstruction with Monotonized Center slope limiter gives better accuracy for both the left-going intermediate shock and the right-going slow shock, in comparison to the second order scheme of BA (which employs a MinMod limiter on magneto-sonic shocks and a special steepening algorithm for linearly degenerate characteristic variables, i.e. Alfvénic and contact discontinuities, actually switched off for compound waves). As we can see, the total absence of characteristic waves decomposition in our code does not prevent at all the sharp definition of discontinuities. Moreover, oscillations due to high

order reconstruction and to the use of the most compressive MC limiter, evident in the v_x profile, are kept at a very low level, while, at the same time, transitions between constant states and rarefaction waves are rather sharp.

A couple of blast wave examples are shown in Fig. 2, again taken from BA, the first with a moderate pressure jump and the second with jump as large as 10^4 , producing a relativistic flow with a maximum Lorentz factor of $\gamma \approx 3.4$. Also in these cases our results are basically equivalent to those in BA, in spite of some small spurious overshoots (more apparent in the ρ profile in the upper panel and in the γ profile of the second panel), due to the compressive limiter, and of a rather poorly resolved contact discontinuity (in the first test, in the second the density peak is far too narrow to recognize it), due to the fact that we cannot steepen it artificially because our component-wise reconstruction. Again, oscillations are nearly absent and rarefaction waves are very well defined. The performances on this kind of tests mainly depend on the limiter choice and on the reconstruction order, so both accuracy and numerical problems are similar to those already shown in the RHD case.

Finally, in Fig. 3 we show the fourth test proposed by BA, which is the magnetic extension of the shock reflection problem of Paper I. To reduce post-shock oscillations, more evident in the pressure profile, we have run this test at second order, thus as in BA; in spite of this our slow shocks are better resolved and the wall heating problem produces a lower dip in the density profile at $x = 0.5$. We have also run this test by using highly

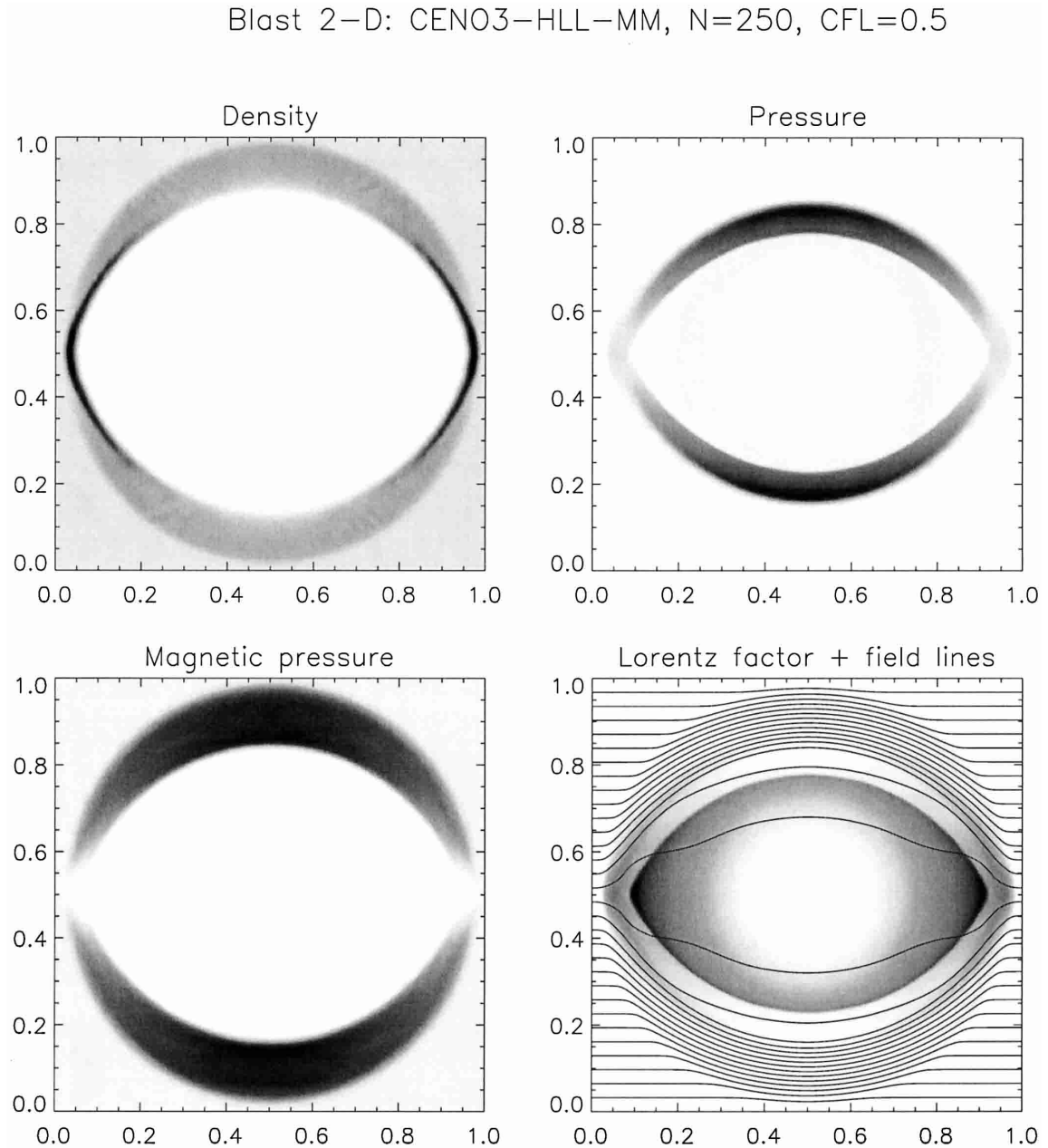


Fig. 4. A RMHD 2-D strong explosion with a pressure jump as high as 10^5 . The resolution is $N_x = N_y = 250$ grid points, and the base multidimensional scheme employing HLL solver and MM limiter is used. Grayscale levels are displayed for density, kinetic pressure, magnetic pressure, and Lorentz factor (together with field lines), where $5.36 \times 10^{-3} \leq \rho \leq 5.79$, $0.0 < p \leq 45.2$, $4.32 \times 10^{-2} \leq p_m \leq 72.2$, and $1.0 \leq \gamma \leq 4.35$.

relativistic flows with $\gamma \approx 224$, as in Paper I, and we have not met any particular problem. The good performance of our code in this last test, in its second order version, is due to the use of the HLL solver which is not based on the definition of an intermediate state, based on the left and right reconstructed quantities, for the definition of characteristic speeds, as it is done in usual Roe-type solvers.

4.2. Multidimensional tests

For truly multidimensional RMHD tests, analytic solutions are not available and so the verification of the code must be done

at a rather qualitative level. Here we will present a cylindrical blast explosion, a cylindrical rotating disk, both in 2-D Cartesian coordinates with a uniform magnetized medium, and the same astrophysical jet of Paper I in cylindrical coordinates, now propagating in a magnetized background. The only other 2-D RMHD code for which extensive numerical verification is available in the literature is KO, where two blast explosions and a Cartesian 2-D jet were tested, in addition to some simulations of simple 1-D waves and shocks on a 2-D grid which will not be repeated here.

In the first test we use the standard $[0, 1] \times [0, 1]$ Cartesian grid, here with a resolution of $N_x = N_y = 250$ grid points, and

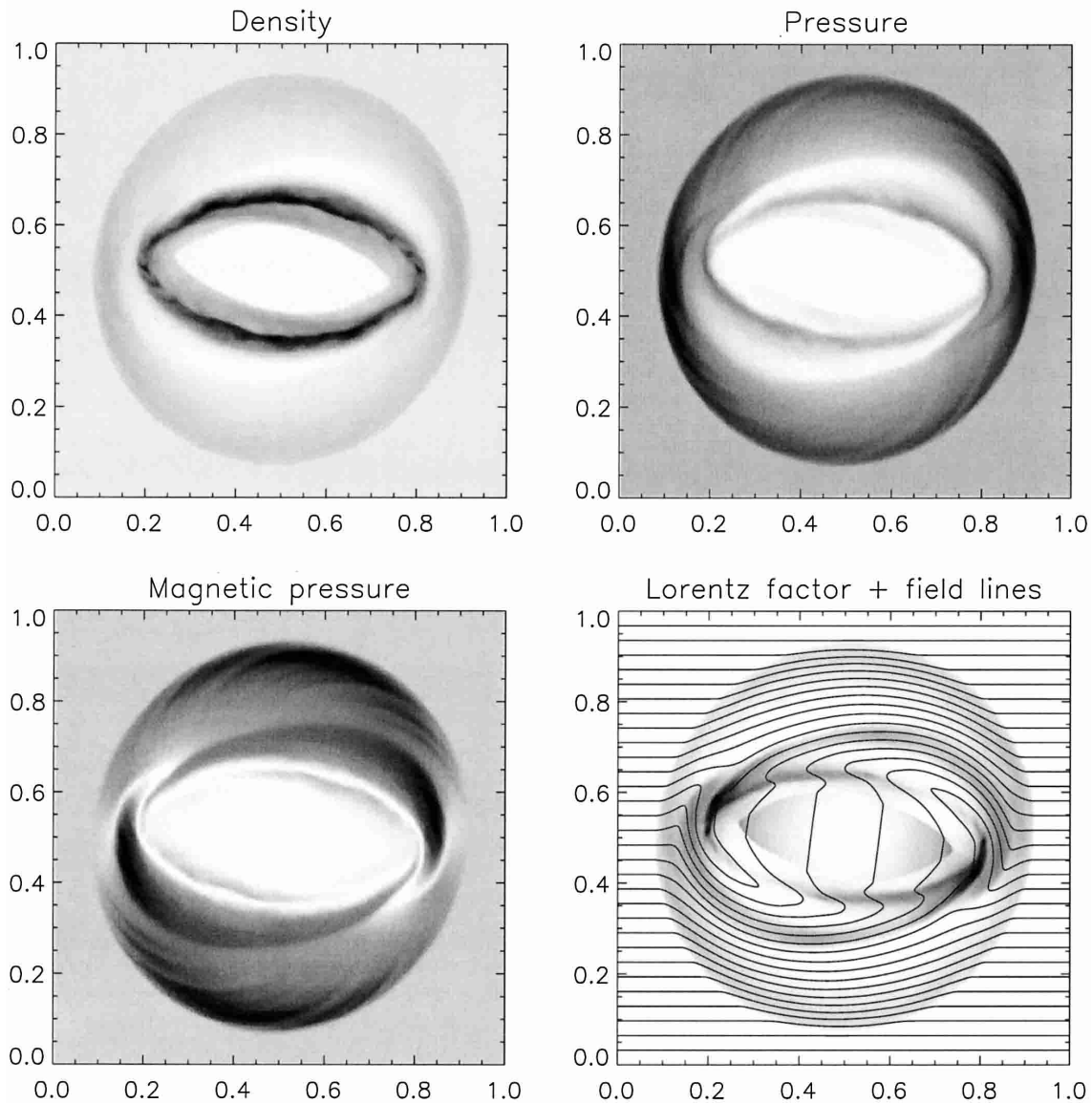
Rotor: CENO3–HLL–MM, $N=400$, CFL=0.5

Fig. 5. The relativistic analog of the *rotor* test, with an initial maximum Lorentz factor of about 10. A high resolution ($N_x = N_y = 400$ grid points) simulation is shown, with the same numerical settings as in Fig. 4. Grayscale levels are displayed for density, kinetic pressure, magnetic pressure, and Lorentz factor (together with field lines), where $0.35 \leq \rho \leq 8.19$, $5.31 \times 10^{-3} \leq p \leq 3.88$, $3.77 \times 10^{-4} \leq p_m \leq 2.43$, and $1.0 \leq \gamma \leq 1.79$.

we define an initially static background with $\rho = 1.0$, $p = 0.01$ and $B_x = 4.0$. The relativistic flow comes out by setting a much higher pressure, $p = 10^3$, within a circle of radius $r = 0.08$ placed at the center of the domain. Here we use $\Gamma = 4/3$ to reduce plasma evacuation at the center. In Fig. 4 we show the situation at $t = 0.4$, when the flow has almost reached the outer boundaries. The flow speed reaches its maximum value along the x direction, $\gamma_{\max} \simeq 4.35$, because the expansion of the blast wave is not slowed down by the presence of a transverse magnetic field, as it happens along y where field lines are squeezed producing the highest magnetic pressure. Magnetized cylindrical blast wave are a nice tool to investigate the behavior of the

plasma, and the robustness of the code, in a variety of degenerate cases (see KO for a detailed description of the various types of shocks involved). In this simulation we can see that, despite the absence of appropriate Riemann solvers handling the degeneracies, our code gives smooth and reasonable results in all directions. If we compare with the results shown by KO, we may see that in spite of the absence of additional artificial resistivity and of the smoothing of the initial structure (both included in KO), our results are rather smooth. Only low-level noise in the density may be seen in the expanding density shell near the diagonals, reminiscent of the *numerical artifacts* found by KO in a run without resistivity. These errors are possibly due

to the use of Cartesian geometry, since numerical errors on the independent v_x and v_y reconstructions are the largest precisely along diagonals.

Another point raised by KO is the possibility of non-strict total energy conservation even in CT upwind MHD schemes, since magnetic field components are stored and evolved at different locations rather than at cell centers where fluid variables are defined. However, if the total energy, which obviously is a conservative variable, is not re-defined in order to prevent unphysical states, it must be globally conserved algebraically. We have checked that in this 2-D test the total energy is conserved within machine accuracy, as expected. In our opinion, the results found by KO in his set of analogue tests, where the total energy is shown to decrease in time (up to a value as large as 3% in the intermediate case, see his Fig. 12), are mainly due to the presence of a non-consistent treatment of the artificial resistivity, which is absent in our code.

The same numerical parameters, but with a higher resolution ($N_x = N_y = 400$), are employed in the second simulation, here adapted to the relativistic case from the classical MHD one (Balsara & Spicer 1999b; LD; Tóth 2000). A disk of radius 0.1 with higher density, $\rho = 10$, rotating at high relativistic speed, $\omega = 9.95 \Rightarrow \gamma_{\max} \simeq 10.0$, the *rotor*, is embedded in a static background with $\rho = 1.0$, $p = 1.0$ and $B_x = 1.0$ ($\Gamma = 5/3$). In Fig. 5 the complicated pattern of shocks and torsional Alfvén waves launched by the rotor may be seen at the usual output time $t = 0.4$, when the central field lines are rotated of an angle of almost 90° . This magnetic braking slows down the rotor, whose maximum Lorentz at the output time is just $\gamma = 1.79$. Note how the initial high density central region has been completely swept away: the density has now its minimum ($\rho = 0.35$) at the center and the material has gone to form a thin oblong-shaped shell. In spite of the presence of very strong shear flows (again, no smoothing is applied to the disk boundary in the initial conditions), it appears that our central high order HLL solver is good enough both in providing high accuracy on smooth waves and in preventing numerical oscillations at shocks. The turbulent aspect of the high density shell should be due to the nonlinear evolution of shear-flow instabilities, since its position coincide with the transition layer where the flow changes its direction from tangential to radial.

Finally, for a truly astrophysical application and as a test of the ENO-CT scheme in a non-Cartesian geometry, we simulate the propagation of a relativistic axisymmetric jet in cylindrical coordinates. The initial settings are taken the same as in Paper I, for ease of comparison with the non-magnetized case. These are a domain $[0, 20]$ along z ($N_z = 400$) and $[0, 8]$ along r ($N_r = 160$), corresponding to a common resolution of 20 grid points per inlet radius, a static background plasma with $\rho = 10.0$, $p = 0.01$, $B_z = 0.1$ ($\Gamma = 5/3$), and jet parameters of $v_z = 0.99$ and $\rho = 0.1$, while pressure and magnetic fields are the same as in the external medium, corresponding to a density ratio $\eta = 1/100$ and to a relativistic Mach number $M = \gamma v / \gamma_{cs} c_s = 18.3$ and to a relativistic Alfvénic Mach number $M_A = \gamma v / \gamma_{cA} c_A = 24.3$, where $c_s^2 = \Gamma p / w_{\text{tot}}$ and $c_A^2 = B^2 / w_{\text{tot}}$. Boundary conditions are reflective at the axis and extrapolation is assumed across the other boundaries. In

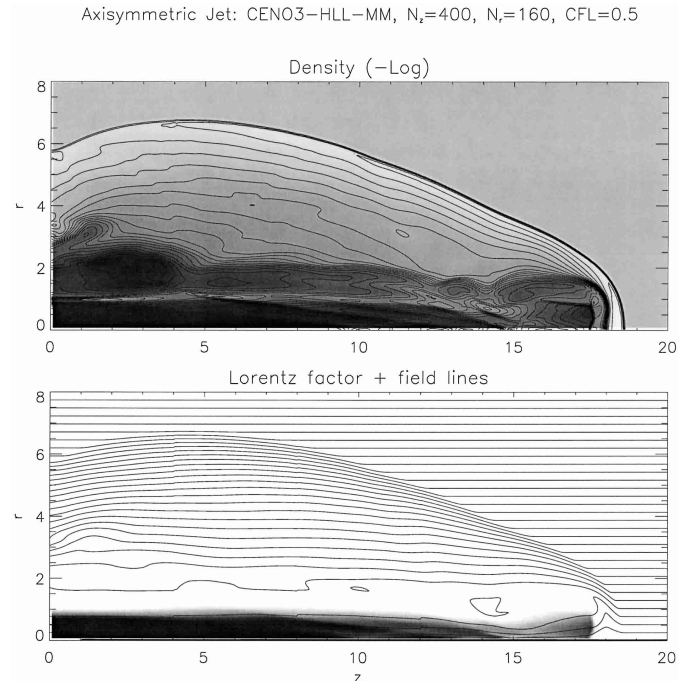


Fig. 6. Magnetized axisymmetric jet simulation in cylindrical coordinates z and r , with $N_z = 400$ and $N_r = 160$ (20 grid points per inlet radius are employed). The evolution is shown here for $t = 35$, with the same settings as in Figs. 4 and 5. In the top panel grey-scale shades and contours are displayed for $-\text{Log}_{10}(\rho)$, with $\rho_{\min} \simeq 0.095$ (black) and $\rho_{\max} \simeq 38.6$ (white). In the bottom panel Lorentz factor and the magnetic field lines are displayed together, where $\gamma_{\max} \simeq 7.14$ (black).

the region $0 < z < 1$, $0 < r < 1$, the initially smoothed jet values are kept constant in time.

The evolution is shown in Fig. 6 at $t = 35$, where the density logarithm, the Lorentz factor and the magnetic field lines are displayed. Note that the head of the jet moves faster than in the non-magnetized case, because of the confinement due to the compressed magnetic field lines (initial equipartition is assumed, so $B^2 = p$) that also reduces the extension of the *cocoon* and stabilizes Kelvin-Helmoltz instabilities, so nicely defined in Paper I. Additional reasons for this latter aspect are of numerical type: the use of MM rather than MC slope limiter and the higher numerical viscosity, due to the magnetic contribution in the fast magneto-sonic speeds, introduces extra smoothing of contact discontinuities.

As we can see from this set of 2-D examples (the 3-D case does not present any additional difficulty), our code is able to obtain similar results to those shown in KO. Like in the fluid case, we have found that the higher order of the scheme can compensate the lack of characteristic waves decomposition. Even the physical limits that the code is capable to cope with look very similar to both KO and Koide et al. (1996), essentially because of errors in reconstruction of multi-dimensional vectors. In fact, separate 1-D reconstruction on vector components may easily produce unphysical states, for example v^2 may be greater than one or the errors on B^2 , needed for fluxes and Alfvénic or magneto-sonic speed calculations, may be too large leading to states with superluminal characteristic modes. While the former problem may be cured by eliminating the

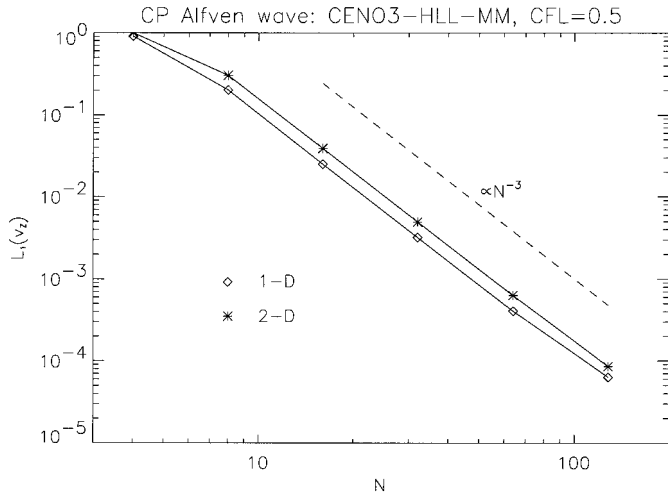


Fig. 7. Convergence test for the 1-D and 2-D CP Alfvén wave problem. Relative L_1 errors on v_z are shown in logarithmic scale. Note that the code soon achieves third order convergence in both cases. The errors in the 2-D case are larger because two periods fit on the main diagonal. The last point in the 1-D case refers to a slightly larger error than expected for perfect third order accuracy, because relativistic effects begin to appear on the wave profile and we are no longer comparing with the correct solution.

reconstruction in some cases, the latter is more difficult to prevent. Another problem, common to classical MHD (see Balsara & Spicer 1999a), appears in situations of low-beta plasma, where $\beta = p/B^2$. When the magnetic field is too strong, the pressure is derived numerically as a difference of two very large numbers (the total energy and the magnetic pressure), so it may even become negative. In our code, when the routine described in Sect. 2.3 still manages to find a solution for v^2 but then negative pressures are found, we reset p to a small value (10^{-6}). The lowest value of the plasma beta that the code is able to handle, when relativistic flows are present, appears to be around $10^{-3} - 10^{-4}$. Typical critical situations are strong rarefactions, as in the 2-D blast wave presented above.

4.3. Convergence tests

The tests presented in the previous subsections were mainly devoted to show the robustness of the code on highly relativistic flows and shocks, thus also proving the useful property of the CENO3 reconstruction algorithm to reduce itself to lower orders near discontinuities, avoiding oscillations typical of high-order central-type schemes. In the present subsection we check the high resolution properties of the interpolation routines on smooth fields. In cases where discontinuous features are absent, these algorithms are designed to achieve third order accuracy. However, the reader might wonder whether the overall RMHD scheme itself, which is based on a rather complicated sequence of CENO3 reconstruction and derivation routines, especially in the multidimensional case, is really able to preserve global third order accuracy properties in both time and space.

To this purpose let us study the propagation of a monochromatic relativistic circularly polarized (CP) Alfvén wave. In the limit of small amplitudes the total magnetic field

strength is preserved in time, the Alfvén speed is given by $B_0/\sqrt{w_{\text{tot}}}$ and the relation between velocity and magnetic fluctuations reduce to $\delta\mathbf{v} = \pm\delta\mathbf{B}/\sqrt{w_{\text{tot}}}$, similarly to the classical MHD case. Define now, at $t = 0$, the various quantities in a generic cartesian reference frame (ξ, η, ζ) as $\rho = 1$, $p = 0.1$, $v_\xi = 0$, $B_\xi = B_0 = 1$, and

$$v_\eta = -B_\eta = A \cos(2\pi\xi), \quad v_\zeta = -B_\zeta = A \sin(2\pi\xi), \quad (46)$$

where we have taken $A = 0.01$. In the 1-D case we simply have $(\xi, \eta, \zeta) = (x, y, z)$, whereas in the 2-D case we consider propagation along the $x = y$ direction, so that $(\xi, \eta, \zeta) = ((x + y)/\sqrt{2}, (-x + y)/\sqrt{2}, z)$. In both cases $[0, 1]$ intervals and periodic boundary conditions have been assumed, so that after one period $t = T$ the wave should return unchanged to the initial position, as long as transverse relativistic effects can be neglected (they scale as $A^2 = 10^{-4}$). In 1-D $B_0 = 1$ and the wave period is $T = 1$, while in 2-D we take $B_0 = \sqrt{2} \Rightarrow B_{0x} = B_{0y} = 1$, so that two complete spatial periods are set along the main diagonal $x = y$ and therefore $T = 0.5$.

Third order convergence, in time and space, can thus be proved by measuring relative errors of a certain quantity, v_z in our case, at different resolutions, where the error is here evaluated as the L_1 norm of the numerical solution after one period T , compared to the initial settings:

$$L_1(v_z) = \frac{\sum_{ij} |v_z(x_i, y_j, t = T) - v_z(x_i, y_j, t = 0)|}{\sum_{ij} |v_z(x_i, y_j, t = 0)|}. \quad (47)$$

In Fig. 7 the errors are plotted in both 1-D and 2-D cases as a function of the number of grid points employed $N = N_x = N_y$, in logarithmic scale. As expected, third order accuracy is achieved, already in low resolution runs. The base scheme employed is CENO3-HLL-MM, which gives the smoothest profiles, more appropriate to wave-like features. However, we have also tested the sharper MC limiter: third order accuracy is globally preserved, but the behavior of the relative errors is more oscillatory, probably due to artificial compression that tends to sharpen somehow even sinusoidal waves (see Fig. 5 of Paper I).

5. Conclusions

The shock-capturing 3-D MHD scheme of Londrillo & Del Zanna (2000) is applied to the special relativistic case, thus extending the code for relativistic gasdynamics described in Del Zanna & Bucciantini (2002), Paper I, to the magnetic case. This is the first higher than second order (third) upwind scheme developed for RMHD, to which high resolution Godunov-type methods have started to be applied only very recently. Instead of defining complicated linearized Riemann solvers, usually based on reconstructed characteristic fields, our scheme just uses the local fastest characteristic velocities to define a two-speed HLL-type Riemann solver. Moreover, reconstruction is applied component-wise, thus time-consuming spectral decomposition is avoided completely, in the spirit of the so-called central schemes. This is of particular importance in both MHD and RMHD, since we do not need to worry about ubiquitous degenerate cases, usually handled in Roe-type schemes by adding artificial numerical viscosity.

A main feature of our code is the correct treatment of the solenoidal constraint, which is enforced to round-off machine errors by extending the constraint transport (CT) method, originally developed for the induction equation alone, to the overall RMHD system: the flux functions are correctly defined by using the staggered magnetic field components, thus avoiding the onset of monopoles even at discontinuities. It is important to notice that, in order to obtain such results, $\nabla \cdot \mathbf{B}$ must be kept equal to zero at cell centers and it must be calculated by using the same staggered components which are evolved in time and the same discretizations applied to flux derivatives (see Tóth 2000, for examples where these properties do not apply). Moreover, numerical fluxes based on four-state reconstructed quantities are defined for the induction equation and here applied to a two-speed central-upwind solver for the first time. In our opinion, to date our method is the only consistent application of CT to an upwind scheme for mixed systems of hyperbolic and Hamilton-Jacobi equations, like MHD and RMHD.

Particular attention has been also devoted to the numerical method needed to derive primitive variables from the set of conservative ones. The 5×5 system of nonlinear equation is reduced to just a *single* equation for the square of the velocity. This is then solved via a Newton-Raphson iterative root-finding algorithm, and analytical expressions are provided for the function whose zeroes are looked for and for its first derivative. This procedure is extremely efficient and robust, and may be used in all RMHD codes, regardless of the numerical scheme employed.

The code is verified against 1-D shock tube tests and 2-D problems, even in non-Cartesian geometries, showing accurate results and non-oscillatory profiles. The code is very robust within the limits imposed by the intrinsic numerical precision, which for multidimensional relativistic flows appear to be $\gamma \sim 10\text{--}20$ ($\gamma > 200$ is reached in 1-D calculations) and $\beta = p/B^2 \sim 10^{-4}\text{--}10^{-3}$. These limits seem to be common to all other existing RMHD codes, and are essentially due to the fact that physical states become undistinguishable in the ultra-relativistic regime (e.g. all characteristic speeds collapse onto the speed of light), where even very small errors on the reconstruction produce fluxes that lead to unphysical states. Typical situations where the code may fail are strong rarefactions in a strongly magnetized medium.

Finally, generalized orthogonal curvilinear coordinates are defined in the code, and presented in the appendix, so our scheme may be easily extended to include General Relativity effects with a given metric.

Acknowledgements. The authors thank the referee, C. Gammie, for his useful comments and especially for asking us to include the convergence tests. This work has been partly supported by the Italian Ministry for University and Research (MIUR) under grants Cofin2000-02-27 and Cofin2001-02-10.

Appendix A: Orthogonal curvilinear coordinates

The equations for special relativistic MHD in a generalized orthogonal curvilinear coordinate system (x^1, x^2, x^3) are obtained by assuming a (covariant) metric tensor of the form

$$g_{\alpha\beta} = \text{diag} \{-1, h_1^2, h_2^2, h_3^2\}. \quad (\text{A.1})$$

The first step is to re-define vector and tensor covariant or contravariant components as *ordinary* components, then spatial differential operators must be converted in this new coordinate system. The set of conservative equations in the divergence form, Eq. (8), becomes

$$\frac{\partial \mathbf{u}}{\partial t} + \frac{1}{h_1 h_2 h_3} \sum_{i=1}^3 \frac{\partial}{\partial x^i} \left(\frac{h_1 h_2 h_3}{h_i} \mathbf{f}^i \right) + \mathbf{g} = 0, \quad (\text{A.2})$$

where \mathbf{u} and \mathbf{f}^i are still those defined in Eqs. (9) and (10), respectively. The source term \mathbf{g} contains the derivatives of the metric elements

$$\mathbf{g} = \begin{pmatrix} 0 \\ h_{12}T_{12} + h_{13}T_{13} - h_{21}T_{22} - h_{31}T_{33} \\ h_{23}T_{23} + h_{21}T_{21} - h_{32}T_{33} - h_{12}T_{11} \\ h_{31}T_{31} + h_{32}T_{32} - h_{13}T_{11} - h_{23}T_{22} \\ 0 \end{pmatrix}, \quad (\text{A.3})$$

where $T_{ij} = w_{\text{tot}} u_i u_j - b_i b_j + p_{\text{tot}} \delta_{ij}$ is the stress tensor and where we have defined

$$h_{ij} = \frac{1}{h_i h_j} \frac{\partial h_j}{\partial x^i}. \quad (\text{A.4})$$

Concerning the magnetic evolution equations, since in our CT scheme we have assumed \mathbf{A} as a primary variable, evolved in time by Eq. (13), the only changes occur in the derivation of the magnetic field:

$$B_i = \frac{h_i}{h_1 h_2 h_3} \sum_{jk} \epsilon_{ijk} \frac{\partial}{\partial x^j} (h_k A_k), \quad (\text{A.5})$$

which just expresses $\mathbf{B} = \nabla \times \mathbf{A}$ in generalized orthogonal coordinates.

In the code, the various combinations of the metric elements are preliminarily calculated and stored on the required grids. Thus $(h_1 h_2 h_3)^{-1}$ and the six h_{ij} terms are defined at grid points $P_{i,j,k}$, $h_2 h_3$ and its reciprocal are defined at the staggered grid $P_{i+1/2,j,k}$ (similarly for $h_3 h_1$ and $h_1 h_2$), where the corresponding flux and longitudinal divergence-free magnetic field component need to be calculated, and finally the h_i elements are stored on the same grids where A_i and E_i are defined, that is h_1 on $P_{i,j+1/2,k+1/2}$ and so on. Thus, to obtain the derivatives in the above expressions, we just need to multiply numerical fluxes and potential vector components with the corresponding geometrical terms, and then we may proceed in the usual way.

References

- Abramowitz, M., & Stegun, A. 1965, Handbook of Mathematical Functions (New York: Dover)
- Aloy, M. A., Ibañez, J. M., Martí, J. M., & Müller, E. 1999, ApJS, 122, 151
- Anile, M. 1989, Relativistic Fluids and Magneto-Fluids (Cambridge: Cambridge University Press)
- Anile, M., & Pennisi, S. 1987, Ann. Inst. Henri Poincaré, 46, 127
- Balsara, D. S. 1994, J. Comput. Phys., 114, 287
- Balsara, D. S., & Spicer, D. S. 1999a, J. Comput. Phys., 148, 133
- Balsara, D. S., & Spicer, D. S. 1999b, J. Comput. Phys., 149, 270

- Balsara, D. S. 2001, *ApJS*, 132, 83 (BA)
- Barmin, A. A., Kulikovskiy, A. G., & Pogorelov, N. V. 1996, *J. Comput. Phys.*, 126, 77
- Begelman, M. C., Blandford, R. D., & Rees, M. J. 1984, *Rev. Mod. Phys.*, 56, 255
- Brackbill, J. U., & Barnes, D. C. 1980, *J. Comput. Phys.*, 35, 426
- Brio, M., & Wu, C. C. 1988, *J. Comput. Phys.*, 75, 400
- Dai, W., & Woodward, P. R. 1998, *ApJ*, 494, 317
- Del Zanna, L., & Bucciantini, N. 2002, *A&A*, 390, 1177 (Paper I)
- Dolezal, A., & Wong, S. S. M. 1995, *J. Comput. Phys.*, 120, 266
- Donat, R., Font, J. A., Ibañez, J. M., & Marquina, A. 1998, *J. Comput. Phys.*, 146, 58
- Duncan, G. C., & Hughes, P. A. 1994, *ApJ*, 436, L119
- Evans, C., & Hawley, J. F. 1988, *ApJ*, 332, 659
- Eulderink, F., & Mellema, G. 1994, *A&A*, 284, 654
- Falle, S. A. E. G., & Komissarov, S. S. 1996, *MNRAS*, 278, 586
- Font, J. A., Ibañez, J. M., Marquina, A., & Martí, J. M. 1994, *A&A*, 282, 304
- Koide, S., Nishikawa, K.-I., & Mutel, R. L. 1996, *ApJ*, 463, L71
- Koide, S., Shibata, K., & Kudoh, T. 1999, *ApJ*, 522, 727
- Koide, S., Meier, D. L., Shibata, K., & Kudoh, T. 2000, *ApJ*, 536, 668
- Komissarov, S. S. 1999a, *MNRAS*, 303, 343 (KO)
- Komissarov, S. S. 1999b, *MNRAS*, 308, 1069
- Kurganov, A., Noelle, S., & Petrova, G. 2001, *SIAM J. Sci. Comput.*, 23, 707
- Liu, X.-D., & Osher, S. 1998, *J. Comput. Phys.*, 142, 304
- Londrillo, P., & Del Zanna, L. 2000, *ApJ*, 530, 508 (LD)
- Marquina, A., Martí, J. M., Ibañez, J. M., Miralles, J. A., & Donat, R. 1992, *A&A*, 258, 566
- Meier, D. L., Koide, S., & Uchida, Y. 2001, *Science*, 291, 84
- Mészáros, P., & Rees, M. J. 1992, *MNRAS*, 258, 41
- Mirabel, I. F., & Rodríguez, L. F. 1994, *Nature*, 371, 46
- Myong, R. S., & Roe, P. L. 1998, *J. Comput. Phys.*, 147, 545
- Nishikawa, K.-I., Koide, S., Sakai, J.-I., et al. 1998, *ApJ*, 498, 166
- Press, W. H., Flannery, B. P., Teukolsky, S. A., & Vetterling, W. T. 1986, *Numerical Recipes* (Cambridge University Press)
- Powell, K. G. 1994, ICASE Tech. Rep. 94-24, NASA Langley Research Center, VA
- Ryu, D., Miniati, F., Jones, T. W., & Frank, A. 1998, *ApJ*, 504, 244
- Roe, P. L., & Balsara, D. S. 1996, *SIAM J. Num. Anal.*, 56, 57
- Schneider, V., Katscher, U., Rischke, D. H., et al. 1993, *J. Comput. Phys.*, 105, 92
- Shu, C.-W. 1997, ICASE Rep. 97-65, NASA Langley Research Center, VA
- Shu, C.-W., & Osher, B. 1988, *J. Comput. Phys.*, 77, 439
- Tóth, G. 2000, *J. Comput. Phys.*, 161, 605